



Supplementary Materials for

Organic and solution-processed tandem solar cells with 17.3% efficiency

Lingxian Meng, Yamin Zhang, Xiangjian Wan*, Chenxi Li, Xin Zhang, Yanbo Wang, Xin Ke, Zuo Xiao, Liming Ding*, Ruoxi Xia, Hin-Lap Yip, Yong Cao, Yongsheng Chen*

*Corresponding author. Email: yschen99@nankai.edu.cn (Y.C.); xjwan@nankai.edu.cn (X.W.); ding@nanoctr.cn (L.D.)

Published 9 August 2018 on *Science* First Release
DOI: 10.1126/science.aat2612

This PDF file includes:

Materials and Methods
Figs. S1 to S13
Tables S1 to S14
References

Materials and Methods

PTB7-Th (also named as PCE10) was purchased from 1-Material Inc. [6,6]-Phenyl-C71-butyric acid methyl ester (PC₇₁BM) was purchased from American Dye Source, Inc. PBDB-T, O6T-4F were synthesized according to previous reports (31,40). ZnO nanoparticles were synthesized following the literature (41). 1,8-diiodooctane (DIO) and MoO₃ were purchased from Alfa-Aesar. Isopropanol (IPA) and chlorobenzene (CB) were purchased from Sigma-Aldrich. PFN-Br, i.e. poly[(9,9-bis{30-[N,N-dimethyl]-N-ethylammonium}propyl)-2,7-fluorene)-alt-1,4 phenylene]dibromide was purchased from Luminescence Technology Corp. PDINO (perylene diimide functionalized with amino N-oxide) was purchased from SunaTech Inc. All other materials were purchased and used as received.

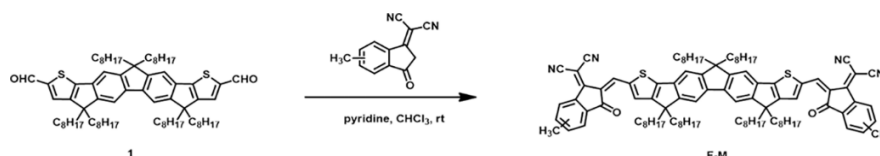
Measurements and instruments

The ¹H and ¹³C nuclear magnetic resonance (NMR) spectra were taken on a Bruker AV400 Spectrometer. Matrix assisted laser desorption/ionization time-of-flight (MALDI-TOF) mass spectrometry were performed on a Bruker Autoflex III instrument. The thermogravimetric analysis (TGA) was carried out on a NETZSCH STA 409PC instrument under purified nitrogen gas flow. UV-Vis spectra was obtained with a JASCO V-570 spectrophotometer. Cyclic voltammetry (CV) experiments were performed with a LK98B II Microcomputer-based Electrochemical Analyzer in dichloromethane solutions. All measurements were carried out at room temperature with a conventional three-electrode configuration employing a glassy carbon electrode as the working electrode, a saturated calomel electrode (SCE) as the reference electrode, and a Pt wire as the counter electrode. Tetrabutyl ammonium phosphorus hexafluoride (n-Bu₄NPF₆, 0.1 M) in dichloromethane was used as the supporting electrolyte, and the scan rate was 100 mV/s. The highest occupied molecular orbital (HOMO) and lowest unoccupied molecular orbital (LUMO) energy levels were calculated from the onset oxidation potential and the onset reduction potential, using the equation $E_{\text{HOMO}} = - (4.80 + E_{\text{ox}}^{\text{onset}})$, $E_{\text{LUMO}} = - (4.80 + E_{\text{re}}^{\text{onset}})$.

The current density-voltage (*J-V*) curves of fabricated devices were obtained by a Keithley 2400 source-measure unit. The photocurrent was measured under AM 1.5G illumination at 100 mW/cm² irradiation using a Enli SS-F5-3A solar simulator, calibrated with a standard Si solar cell (made by Enli Technology Co., Ltd., Taiwan, and calibrated report can be traced to NREL). The thickness of the active layers in the photovoltaic devices was measured under a Veeco Dektak 150 profilometer. The EQE spectrum was measured using a QE-R Solar Cell Spectral Response Measurement System (Enli Technology Co., Ltd., Taiwan). To measure the rear and front cell, light bias obtained by 550 nm low-pass optical filters and 850 nm high-pass were selected to excite (saturate) the front and rear cells, respectively. Electrical biases of 0.7 and 0.9 V were applied on the tandem OSCs to measure the front and rear subcells, respectively (34). The mismatch factor M values of

both subcells under the solar simulator are calculated according to the reference and the values are around 1 (1.007 for the front cell and 1.066 for the rear cell) (42).

Synthesis of F-M (Scheme S1) (32)



Scheme S1. Synthetic route of F-M.

The reaction and manipulation were carried out under argon atmosphere with use of standard Schlenk techniques. The intermediate compound **1** was prepared according to the literature (43).

A solution of compound **1** (120 mg, 0.11 mmol) and Me-INCN (112 mg, 0.54 mmol) in dry CHCl₃ (25 mL) was degassed three times and then 0.2 mL pyridine was added under the protection of argon. After stirring for 24 h at the room temperature, the mixture was poured into CH₃OH (100 mL) and filtered to remove the impurities. The crude product was purified by column chromatography using chloroform as eluent to obtain the target molecule F-M as a black-blue solid (80 mg, 49.3%) (**Scheme S1**). ¹H NMR (400 MHz, CDCl₃): δ 8.96 (s, 2H), 8.57 (d, 1H), 8.50 (s, 1H), 7.82 (d, 1H), 7.71 (s, 3H), 7.69 (s, 2H), 7.61 (d, 2H), 7.56 (m, 2H), 2.57(d, 6H), 2.07 (m, 8H), 1.96 (m, 4H), 1.13 (m, 72H), 0.79 (m, 18H). ¹³C NMR (100 MHz, CDCl₃): δ 188.49, 188.13, 161.51, 161.40, 161.01, 160.97, 156.61, 156.24, 152.25, 146.47, 146.05, 142.34, 140.36, 140.28, 138.30, 137.96, 137.61, 137.33, 136.67, 135.82, 135.31, 134.83, 125.59, 125.18, 123.95, 123.53, 121.78, 121.72, 116.07, 115.14, 115.08, 115.00, 114.45, 67.97, 67.44, 54.65, 54.19, 40.41, 39.17, 31.77, 31.73, 29.97, 29.93, 29.71, 29.28, 29.20, 24.47, 23.90, 22.60, 22.57, 22.10, 14.04. MS (MALDI-TOF): m/z [M+H]⁺ calcd for C₉₉H₁₂₂N₄O₂S₂, 1463.903; found, 1463.908 (6).

Device Fabrication and Optimization

First, the single junction front and rear cells were optimized. For PBDB-T:F-M based single junction cells, the detailed optimization results (through a normal device structure with different donor:acceptor ratio, additive, concentration and spin speed) are shown in Table. S2-Table. S6. Then PBDB-T:F-M based device with an inverted structure was fabricated using the above optimized active layers parameters. The PTB7-Th:O6T-4F:PC₇₁BM or PTB7-Th:O6T-4F based single junction cells optimization followed the literatures (4, 31). The tandem solar cells were optimized through changing the thickness of interconnection layer and active layers of the front and rear cell and the results are shown in the Table. S7-Table. S13.

Fabrication of the single junction devices

The normal structure device of PBDB-T:F-M was fabricated with the structure of ITO/PEDOT:PSS (Clevios PVP Al 4083) /PBDB-T:F-M/PDINO/Al (32). First, A thin layer (20 nm) of PEDOT:PSS was spin cast on top of pre-cleaned ITO substrates and annealed in air at 150 °C for 15 min. The substrates were then transferred into an Ar-filled glove box. Then the blend solution of PBDB-T:F-M (1:1 w/w) (10 mg/mL, from a chlorobenzene (CB) with 0.2% DIO) was spin-coated with different spin speeds. After that, about 5 nm PDINO (dissolved in methanol with the concentration of 1 mg/mL) layer (44) was spin-coated on the top of the active layer. Finally, a layer of Al with thickness of 80 nm was deposited under under 2×10^{-4} Pa.

The inverted structure device of PBDB-T:F-M was fabricated with device architecture of ITO/ZnO/PFN-Br/PBDB-T:F-M/M-PEDOT/Ag. A thick layer of ZnO was deposited by spin-coating a ZnO precursor on top of pre-cleaned ITO substrates at 4000 rpm for 40s followed by annealing at 200°C for 1 h in air. Subsequently, a thin layer of PFN-Br was spin-coated on ZnO for improving the interfacial properties (45). The substrates were then transferred into an Ar-filled glove box. Then the blend solution of PBDB-T:F-M (1:1 w/w) (10 mg/mL, from CB with 0.2% DIO) was spin-coated at 1000 rpm for 40 s to form the active layer. The modified PEDOT:PSS layer (Clevios P VP Al 4083 diluted with equal volume of isopropyl alcohol and 0.3 wt% of Zonyl FSN) (ca. 50 nm) was then spin-coated. After thermally annealed at 120°C for 10 min, an Ag layer (70 nm) were then deposited by vacuum evaporation under 2×10^{-4} Pa through a shadow mask.

For PTB7-Th:O6T-4F:PC₇₁BM or PTB7-Th:O6T-4F based device, the device architecture was ITO/ZnO/active layer/MoO₃/Ag. The active layer was spin-coated at 1600 rpm for 40 s from CB solution (7.2 mg/mL, 1% DIO by volume) with weight ratio of PTB7-Th:O6T-4F:PC₇₁BM at 1:1.05:0.45 or 2200 rpm for 40 s from CB solution (9 mg/mL, 1% DIO by volume) with weight ratio of PTB7-Th:O6T-4F at 1:1. A MoO₃ layer (6 nm) and an Ag layer (70 nm) were then deposited on the active layer by vacuum evaporation under 2×10^{-4} Pa (4).

Fabrication of the tandem devices

The tandem devices were fabricated with an architecture of ITO/ZnO/PFN-Br/PBDB-T:F-M/M-PEDOT/ZnO/ (PTB7-Th:O6T-4F:PC₇₁BM or PTB7-Th:O6T-4F) /MoO₃/Ag. The PBDB-T:F-M active layers were fabricated via the same process as the single cells with different thicknesses. Subsequently, the M-PEDOT layer (ca. 50 nm) was spin-coated on top of the active layer of the front subcell, followed by annealing at 120°C for 10 min, and then ZnO nanoparticles layer (ca.15 nm) was spin-coated and annealed at 120°C for 10 min in glove box. Then, the PTB7-Th:O6T-4F:PC₇₁BM or PTB7-Th:O6T-4F active layers were

fabricated via the same process as the single cells with different thicknesses. A MoO₃ layer (ca.6 nm) and an Ag layer (ca.70 nm) were then deposited on the active layer by vacuum evaporation under 2×10^{-4} Pa. The effective areas of cells were $\sim 4 \text{ mm}^2$ defined by shallow masks. Devices with larger size active area were also fabricated and studied and the results are shown in Table S14.

Light intensity dependence of photovoltaic parameter

In order to investigate the dependence of the J - V measurements under different light intensities, a neutral density sieve was used to modulate the light intensity, and a standard Si solar cell was used to calibrate the light intensity.

As shown in fig. S8, the light intensity dependence of J_{sc} , V_{oc} and FF of the tandem cells shows similar behavior to those reported high performance single-junction devices, i.e. the fact that the J_{sc} is proportional to illuminated light intensity, indicating there is no substantial space charge buildup occurred in the tandem device and the interconnecting layer (15), and the FF increases to 76.8% under the lower light intensity, which is attributed to lower bimolecular recombination of the active layer, and the V_{oc} increases with increasing the light intensity. Clearly, it's indicating that the two subcells performed well and an optimal interconnection layer is achieved (46).

Optical simulations

The optical model was performed based on the Transfer Matrix Formalism model (TMM) and the results are shown in Fig 3C. The refractive index (n) and extinction coefficient (k) spectra of each layer in the devices were measured using a J.A. WOOLAM Co. V-VASE ellipsometer (VB-400 Control Module).

With the measured refractive index (n) and extinction coefficient (k) of all the concerned layers employed in the tandem devices, Fig. 3C displays the simulation results of the dependence of tandem cell J_{sc} versus the thicknesses of the two active layers. Based on the optical simulation, the best J_{sc} would be reached when the thicknesses of the optimized front and rear subcell active layers are around 200 and 120 nm, respectively. With these results and that from the single-junction cell evaluation above, a series of tandem devices were fabricated and studied with different subcells thickness. The thickness of the front subcell active layer was tuned from 120 to 180 nm while keeping the active layer thickness of the rear subcell to be 110 nm. Similarly, the thickness of rear subcell was evaluated in the range from 90 to 110 nm. The detailed photovoltaic parameters are summarized in Table 1 and fig. S8. The tandem devices all showed a V_{oc} of $\sim 1.64 \text{ V}$, approximately equal to the sum of individual V_{oc} of the subcells, indicating an optimal interconnecting layer with negligible potential loss and good ohmic contact (20), while the J_{sc} and FF depended on the thickness of the subcells. For example, when the active layer thickness of the rear

subcell was fixed to 110 nm, the V_{oc} of the tandem cells had negligible change with increasing the thickness of the front cell from 120 to 180 nm, but the J_{sc} showed a maximum value of 14.35 mA/cm² at 150 nm, together with a FF as high as 73.7%. Further increasing the thickness from 150 nm, the J_{sc} has a slight decrease, but the FF decreased significantly. On the other hand, when the active layer thickness of the front subcell was fixed to 150 nm and the rear cell thickness changed from 90 to 125 nm, the tandem devices achieved both a maximum J_{sc} of 14.35 mA/cm² and FF of 73.7% at the 110 nm thickness. Overall, the devices all give excellent performance with PCEs above 15% and a remarkable PCE of 17.36%, with V_{oc} of 1.642 V, J_{sc} of 14.35 mA/cm² and FF of 73.7% is achieved under the optimal conditions.

While over 17% PCE has been achieved here under AM 1.5G, there are still significant potential to achieve much higher performance for tandem OPV device from the perspective of both theory and the state of the art results, where better front and rear subcell active materials with wide and infrared absorption with high and matching EQE response should be the focus in future works.

The semi-empirical model analysis

For the semi-empirical analysis based on a 2-terminal monolithic tandem cell with two subcells in series, the fundamental assumptions are made as follows:

- 1) The interconnection layer is assumed to be an ideal fully transparent intermediate layer with a loss-free recombination of charge carriers.
- 2) An internal quantum efficiency (IQE) of 100% is considered for the whole absorption wavelengths (47).
- 3) EQE is assumed to be same in the whole absorption range with given values 65-85%, which are the state of art results reported in the literature (24, 48).
- 4) It is assumed that there is no absorption overlap between the two subcells. That is, all photons with energy higher than $E_{g,1}$ ($= 1240/\lambda_{onset, front\ cell}$) are absorbed by the front cell, and that with energy between $E_{g,1}$ and $E_{g,2}$ ($= 1240/\lambda_{onset, rear\ cell}$) could be absorbed by the rear cell. The tandem cell $J_{sc, tandem}$ is half of integrated photocurrent from 300 nm to the rear cell absorption onset ($\lambda_{onset, rear\ cell}$) with a given EQE value. The integrated photocurrent of the front cell is assumed to be equal to that of the rear cell for the best performed tandem cell governed by Kirchhoff's law.
- 5) The V_{oc} of the tandem cell is the sum that of each subcell.
- 6) The subcells have FF with values of 65%-80%, which is consistent with the most reported ones in literatures (25).
- 7) In the discussion as follows, the optical gap of the subcell E_g ($= 1240/\lambda_{onset}$) is defined as the narrower optical gaps of the donor-acceptor couples. Note, for the fullerene based devices, the absorption onset is considered to be that of the donor materials. For

the fullerene-free based devices, it referred to be that of material, either donor or acceptor, whichever has a narrower bandgap (23).

Based on above assumptions, the three photovoltaice parameters V_{oc} , J_{sc} and FF of a 2-terminal monolithic tandem cell are obtained as follows:

1) For a rear cell with absorption onset λ_1 , the J_{sc} of the tandem cell could be obtained from equation 1 (Eq. 1).

$$J_{sc, \text{ tandem}} = \frac{1}{2} \cdot \int_{300}^{\lambda_1} \frac{q\lambda}{hc} \cdot E(\lambda) \cdot EQE(\lambda) \cdot d\lambda = \int_{300}^{\lambda_2} \frac{q\lambda}{hc} \cdot E(\lambda) \cdot EQE(\lambda) \cdot d\lambda \quad (1)$$

where $E(\lambda)$ is the spectral irradiance in AM 1.5G, λ_1 and λ_2 are the absorption onset of rear and front cell, h is Planck's constant, c is the speed of light and q is the elementary charge. From the above assumption, the absorption onset (λ_2) of a matched front cell could be determined from Eq. 2 under AM 1.5G light illumination.

$$J_{sc, \text{ front}} = J_{sc, \text{ rear}} = \frac{1}{2} \cdot \int_{300}^{\lambda_1} \frac{q\lambda}{hc} \cdot E(\lambda) \cdot EQE(\lambda) d\lambda = \int_{300}^{\lambda_2} \frac{q\lambda}{hc} \cdot E(\lambda) \cdot EQE(\lambda) \cdot d\lambda \quad (2)$$

2) The V_{oc} of the subcells is determined by the following Eqs. 3 and 4 (23).

$$V_{OC, \text{ front}} = \frac{1}{q} (E_g - E_{loss}) = \frac{1}{q} \left(\frac{1240}{\lambda_2} - E_{loss} \right) \quad (3)$$

$$V_{OC, \text{ rear}} = \frac{1}{q} (E_g - E_{loss}) = \frac{1}{q} \left(\frac{1240}{\lambda_2} - E_{loss} \right) \quad (4)$$

Herein, the front and rear cell are considered to have the same E_{loss} for the calculation simplification. The E_{loss} are assumed to be 0.4-0.8 eV according to overall reported values (26). The V_{oc} of the tandem cell is given by Eq. 5

$$V_{OC, \text{ tandem}} = V_{OC, \text{ front}} + V_{OC, \text{ rear}} = \frac{1}{q} \left(\frac{1240}{\lambda_2} + \frac{1240}{\lambda_1} - 2E_{loss} \right) \quad (5)$$

So for the tandem solar cells, the PCE can be calculated from the Eq. 6 under AM 1.5G light illumination.

$$\begin{aligned} \text{PCE (\%)} &= V_{oc} \cdot J_{sc} \cdot FF / P_{in} \\ &= \frac{1}{q} \left(\frac{1240}{\lambda_2} + \frac{1240}{\lambda_1} - 2E_{loss} \right) \cdot \frac{1}{2} \cdot \int_{300}^{\lambda_1} \frac{q\lambda}{hc} \cdot E(\lambda) \cdot EQE(\lambda) \cdot d\lambda \cdot FF / P_{in} \end{aligned} \quad (6)$$

Fig. S2 shows PCEs of a 2-T monolithic tandem solar cell versus EQE and absorption onset of rear cell with assuming the E_{loss} of each subcell in the range of 0.4-0.8 eV and FF of 0.65-0.80.

Fig. S3 shows PCEs of 2-T monolithic tandem solar cells versus E_{loss} and absorption onset of rear cell with assuming EQE with values of 65%-85% and FF of 0.65-0.80.

As fig.S2G shows that, a PCE of $\sim 20\%$ could be reached if the $\lambda_{onset, rear cell}$ is up to 1100 nm with an average EQE of 75%, FF being 0.75 and a typical E_{loss} of 0.6 eV, which is consistent with other theoretical analysis (16). Clearly, these values could likely be obtained in reality as most of these parameters have been already achieved for various OPV materials and devices (3, 4, 24-26), particularly when considering the wide diversity of organic/polymeric materials including the recent significant development of small molecules/oligomer A-D-A type donors (14, 28, 29) and acceptors (3, 16).

With fixed FF and EQE, PCEs of the tandem devices are determined by E_{loss} and absorption onset of rear cell as shown in fig.S3. Importantly, from these modelling results shown in Fig.1C and fig. S3, E_{loss} seems to make a bigger impact on the overall PCEs. Also, with E_{loss} increasing, the absorption onset of rear cell ($\lambda_{onset, rear cell}$) with the PCE_{max} has a tendency to blue shift. With a certain FF and EQE: 1) when $E_{loss} = 0.4$ eV, the PCE_{max} of $\sim 25.0\%$ was obtained when $\lambda_{onset, rear cell} = 1070-1200$ nm (Fig. 1C); 2) when $E_{loss} = 0.5$ eV, the PCE_{max} of $\sim 22.6\%$ was obtained when $\lambda_{onset, rear cell} = 1060-1125$ nm (Fig. 1C); 3) when $E_{loss} = 0.6$ eV, the PCE_{max} of 20.2% was obtained for $\lambda_{onset, rear cell} = 1030-1100$ nm (Fig. 1C); 4) when $E_{loss} = 0.7$ eV, the PCE_{max} of 17.8% was obtained at a large range for $\lambda_{onset, rear cell} = 900-1100$ nm (Fig. 1C); 5) while when $E_{loss} = 0.8$ eV, the PCE_{max} of 15.8% was obtained for $\lambda_{onset, rear cell} = 900-945$ nm (Fig. 1C). When $\lambda_{onset, rear cell}$ increasing further, the PCE_{max} gradually decreases. Based on these, for tandem OPV devices, the optimal absorption onset of the rear cell is somewhat blueshifted compared with that ~ 1127 nm from SQ studies (25), probably due to the large non-radiative voltage losses result in large E_{loss} for OPV (26).

Material screening

Based on the equation of $PCE = J_{sc} \times V_{oc} \times FF / P_{in}$ (where J_{sc} is the short-circuit current density, V_{oc} is the open circuit voltage, FF is the fill factor and P_{in} is the power density of

the incident light.), to achieve a best PCE under AM 1.5G, all the J_{sc} , V_{oc} and FF need to be maximized simultaneously. In this content, first, the active layers need have both as wide absorption as possible and maximized V_{oc} (meaning minimized E_{loss}). Also, there is a trade-off between the maximized J_{sc} and V_{oc} as the multiplication of these two factors decide the eventual PCEs. Based on these and the equation of

$$J_{sc,tandem} = \frac{1}{2} \times \int_{300}^{\lambda_1} \frac{q\lambda}{hc} \times E(\lambda) \times EQE(\lambda) d\lambda = \int_{300}^{\lambda_2} \frac{q\lambda}{hc} \times E(\lambda) \times EQE(\lambda) d\lambda \quad \text{and}$$

$$V_{oc,tandem} = V_{oc,front} + V_{oc,rear} = \frac{1}{q} \left(\frac{1240}{\lambda_2} + \frac{1240}{\lambda_1} - 2E_{loss} \right) \quad (\text{where } E(\lambda) \text{ is the spectral irradiance}$$

in AM 1.5G, λ_1 and λ_2 are the absorption onset of rear and front cell, h is Planck's constant, c is the speed of light and q is the elementary charge) for tandem cell, the predicted best PCEs should be obtained when the rear cell absorbs up to 1000~1100 nm (i.e. E_g of 1.13~1.24 eV for the rear layer active materials) as shown in Fig. 1. With this, based on the experimental results of a wide range of compounds from literatures and our own testing (3, 4, 16), PTB7-Th was selected as the donor and O6T-4F and PC₇₁BM as the acceptors for the materials of the rear cell (4), as this combination has absorption up to 1050 nm-matching the absorption range above. Also, it has generally high EQE in the long wavelength range (~720 -1050 nm) required for an optimal rear cell and thus a higher J_{sc} of ~27.89 mA/cm² and an integrated current of 11.2 mA/cm² in the range of 720-1050 nm. Note also the individual cell of this active material combination has a decent V_{oc} of ~0.69 eV (with a small E_{loss} of 0.51 eV), and FF of ~69%. With these data, as we indicated in the original manuscript, this is probably the best so far available as rear cell active materials.

Then, the requirements for the front cell materials could be guided and selected based on Fig 1B and S1 and equation of

$$J_{sc,tandem} = \frac{1}{2} \cdot \int_{300}^{\lambda_1} \frac{q\lambda}{hc} \cdot E(\lambda) \cdot EQE(\lambda) d\lambda = \int_{300}^{\lambda_2} \frac{q\lambda}{hc} \cdot E(\lambda) \cdot EQE(\lambda) d\lambda .$$

Based on these, the front cell required for the best performed tandem cell should have material's absorption edge at ~680-720 nm (i.e. E_g of 1.72-1.82 eV). From here, based on large literatures (3, 49) and our own results (32), the pair PBDB-T and F-M were selected as the front cell materials (32), as this combination gave a higher V_{oc} of ~0.94 V, and J_{sc} of 15.96 mA/cm² from 300 to 750 nm (close to the best 720 nm indicated above). Also, the single junction cell of this combination has a high FF of 69%, which is also required to have overall higher PCE for the entire tandem cell. While the E_{loss} for this combination is ~0.71 eV, still not so small, and also with absorption somehow red-shifted to 750 nm compared with the best (720 nm) suggested by the model analysis, but based on the requirements above (E_g of ~1.72 eV indicated by the model analysis, and also as high as possible FF and EQE), this is probably the best to match the selected rear device for high PCE of the entire tandem

cell.

The impact of secondary acceptor PC₇₁BM

As can be seen from fig. S11, the absorption in the long wavelength range (~900-1050 nm) increased for the ternary system. More accurately, the ternary active layer (black plot) has stronger absorption than the binary system (red one) without PC₇₁BM in the range of long wavelength range. The stronger absorption in 900-1050 nm should be mainly due to the morphology change due to the addition of PC₇₁BM as discussed below.

The morphology for the active layers has been studied by using transmission electron microscope (TEM) as earlier reported (4, 31). It has been observed that clearer nanofiber structures were obtained in the ternary blend film. This means that better phase separation should be generated after PC₇₁BM addition, resulting in either larger domain size of the acceptor or better packing between the acceptor molecules. Also, note binary blend film gave a hole mobility (μ_h) of $6.82 \times 10^{-4} \text{ cm}^2 \text{ V}^{-1} \text{ s}^{-1}$ and electron mobility (μ_e) of $3.91 \times 10^{-5} \text{ cm}^2 \text{ V}^{-1} \text{ s}^{-1}$ (31), while the ternary blend film showed a μ_h of $6.35 \times 10^{-4} \text{ cm}^2 \text{ V}^{-1} \text{ s}^{-1}$ and μ_e of $4.80 \times 10^{-4} \text{ cm}^2 \text{ V}^{-1} \text{ s}^{-1}$ (4), indicating a more balanced charge transportation due to a close μ_h/μ_e value in ternary system (decreased from 17 to 1.3). So both the improved absorption in the long wavelength and balanced charge transportation should be the reasons for the increased EQE and J_{sc} in the long wavelength range.

Figures

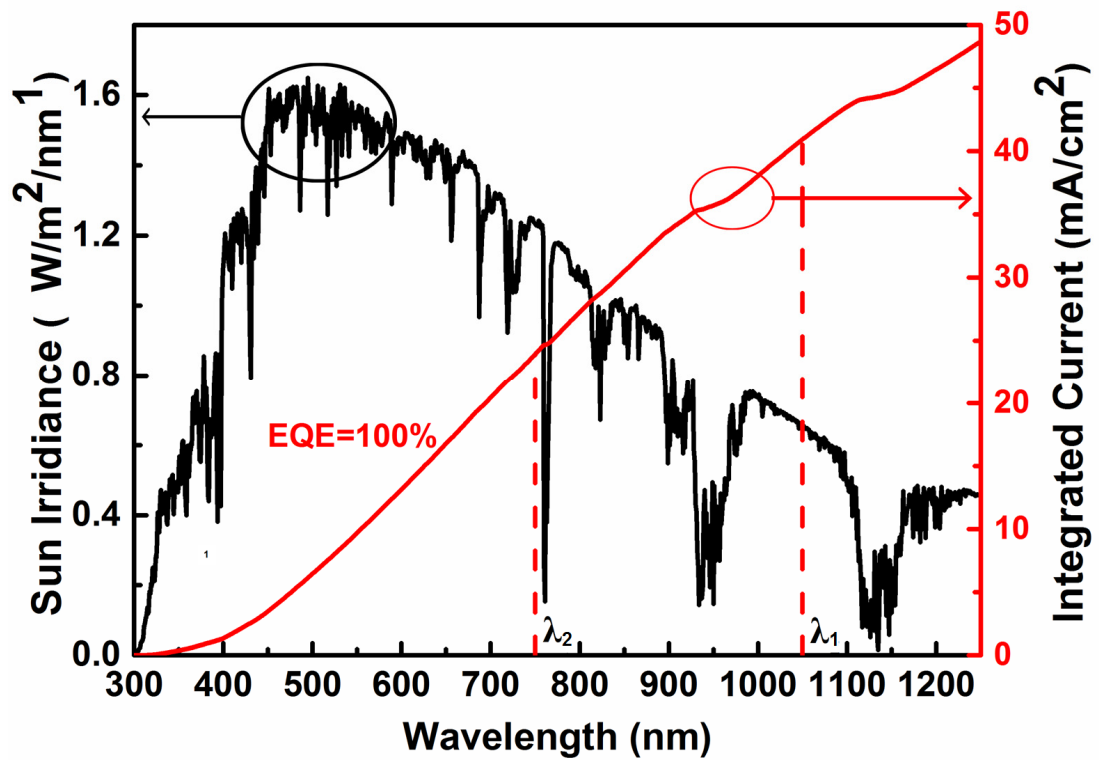


Fig. S1. Sun irradiance (black) as a function of wavelength, and the integral of the curve (red) represents the obtainable theoretical current density with assumption of 100% EQE response.

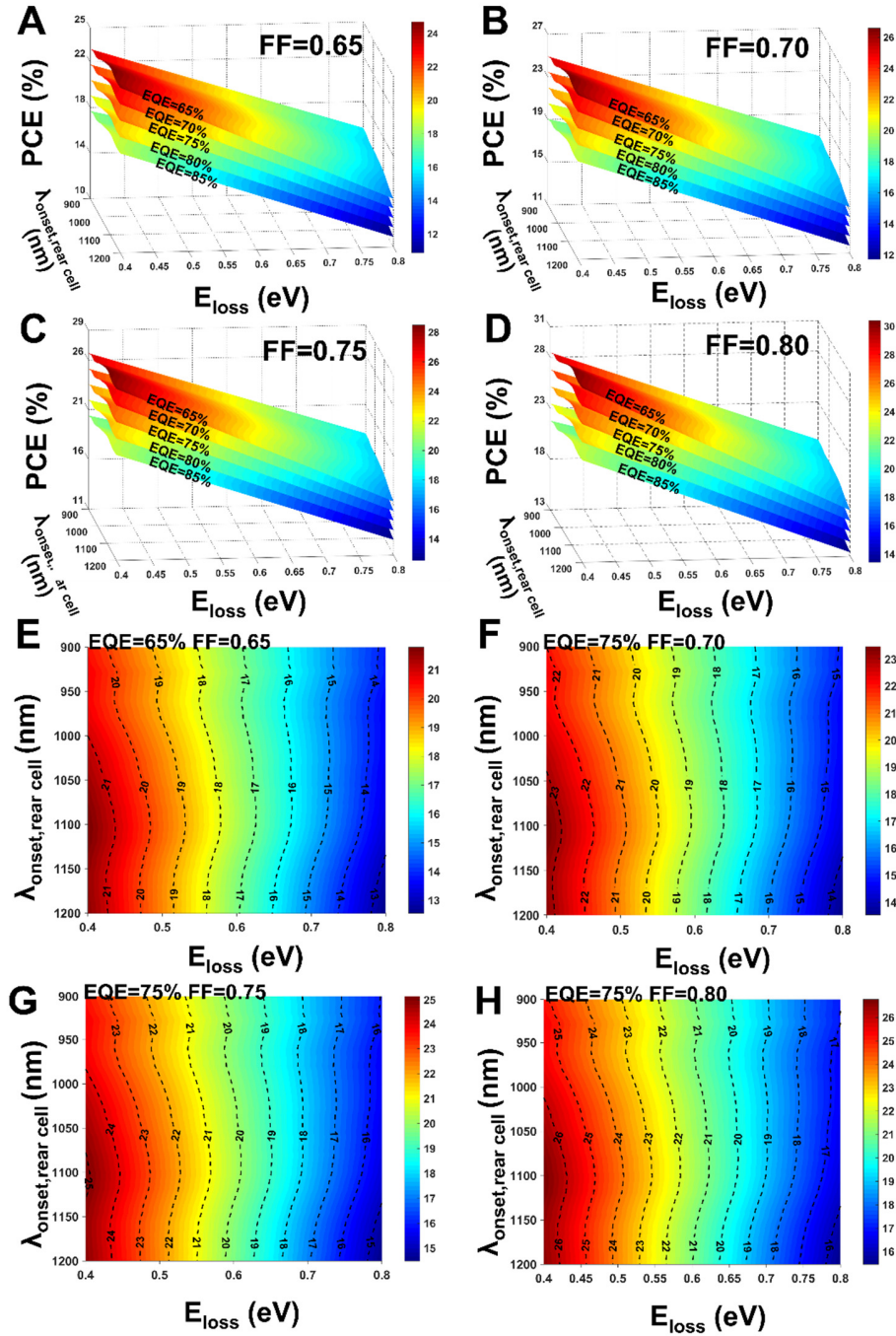


Fig. S2. Predicted PCEs of 2-T monolithic tandem solar cells based on semi-empirical analysis under AM1.5G. (A-D) PCEs versus EQE and $\lambda_{\text{onset, rear cell}}$ with assuming the E_{loss} of each sub cell with value of 0.40-0.80 eV and FF of 0.65 (A), 0.70 (B), 0.75 (C), 0.80 (D); (E-H) PCEs versus E_{loss} and $\lambda_{\text{onset, rear cell}}$ with assumed E_{loss} of 0.60 eV and FF of 0.65 (E), 0.70 (F), 0.75 (G), 0.80 (H).

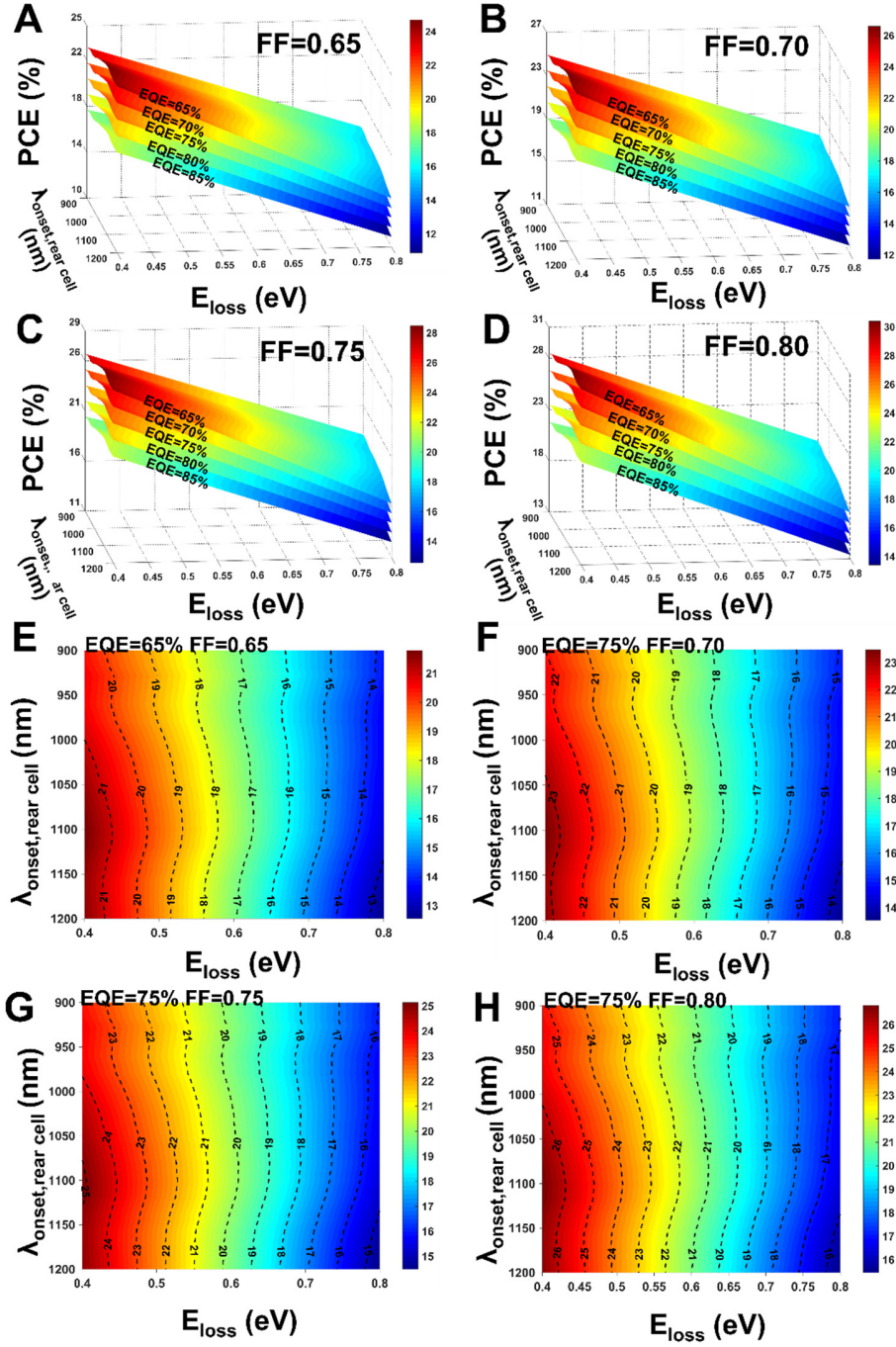


Fig. S3. Predicted PCEs of 2-T monolithic tandem solar cells based on semi-empirical analysis under AM1.5G. (A-D) PCEs versus E_{loss} and $\lambda_{\text{onset, rear cell}}$ with assuming the EQE with value of 65%-80% and FF of 0.65 (A), 0.70 (B), 0.75 (C), 0.80 (D); (E-H) PCEs versus E_{loss} and $\lambda_{\text{onset, rear cell}}$ with assumed EQE of 75% and FF of 0.65 (E), 0.70 (F), 0.75 (G), 0.80 (H).

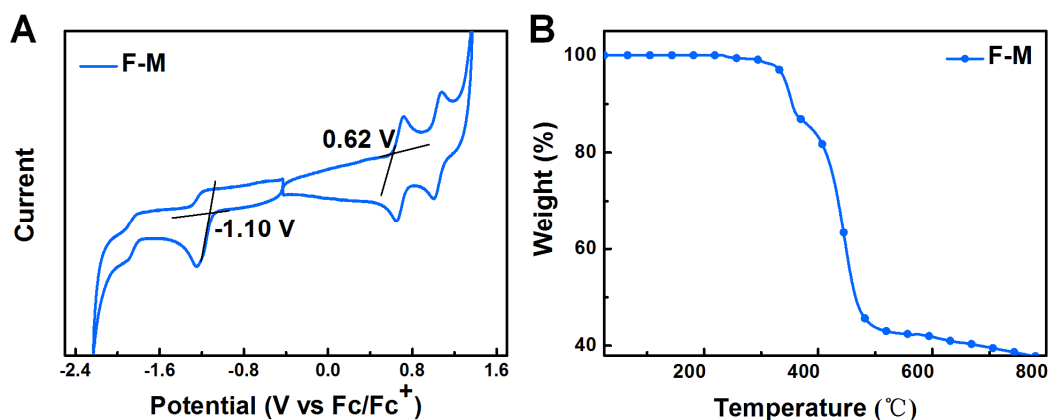


Fig. S4. (A) Cyclic voltammogram of F-M in dichloromethane solution with 0.1 mol/L *n*-Bu₄NPF₆ at a scan rate of 100 mV/s. (B) TGA plot of F-M measured under N₂ atmosphere.

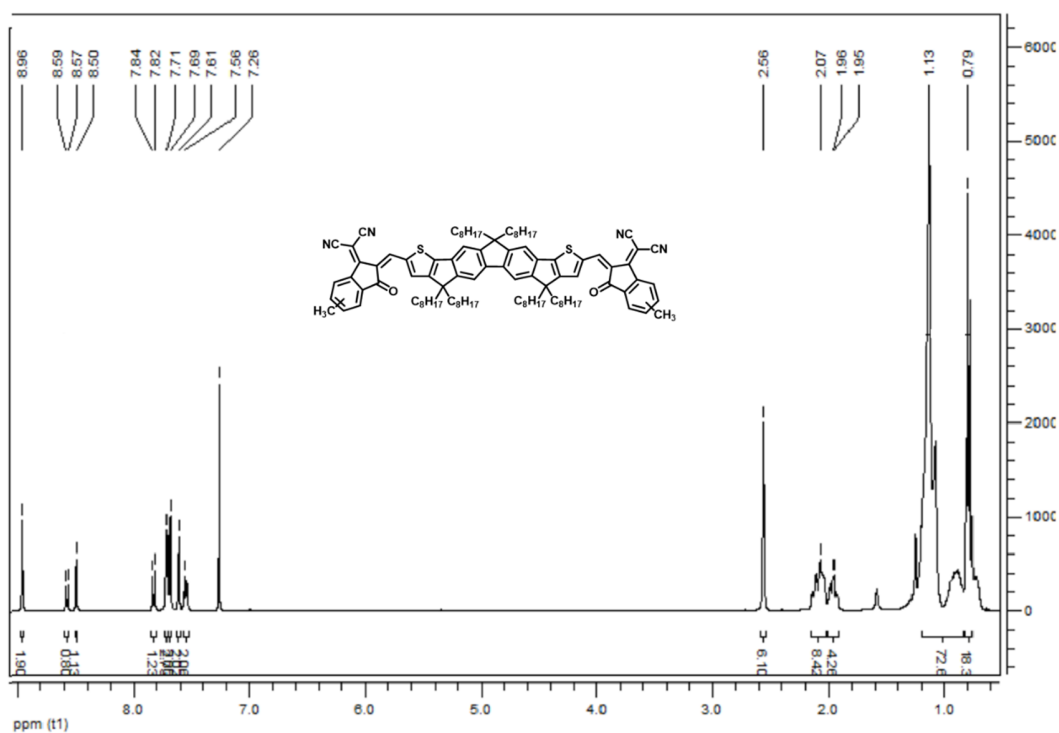


Fig. S5. ¹H NMR spectra of compound F-M in CDCl₃.

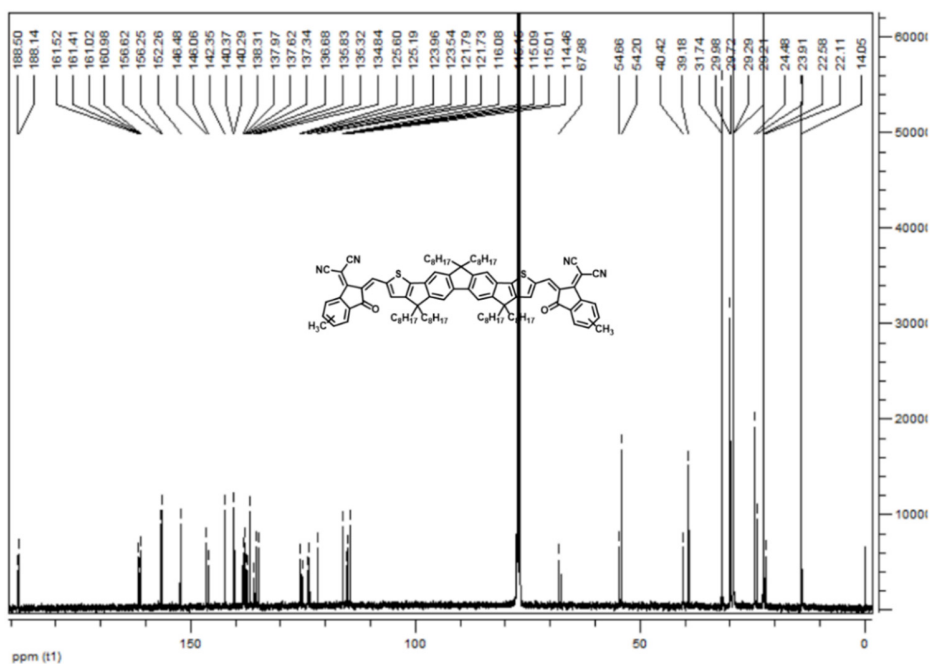


Fig. S6. ^{13}C NMR spectra of compound F-M in CDCl_3 .

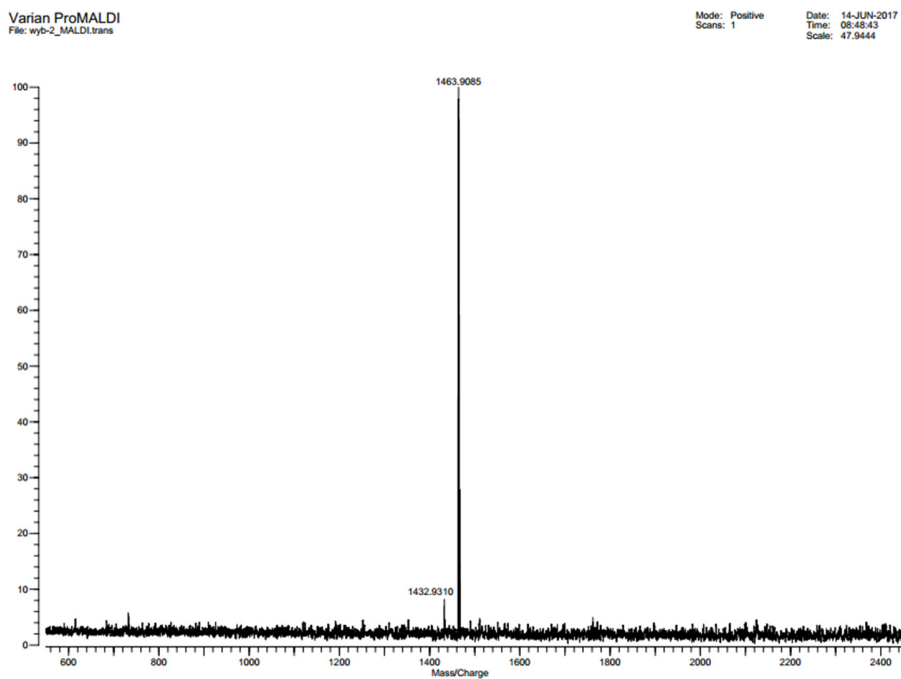


Fig. S7. MALDI-TOF of F-M.

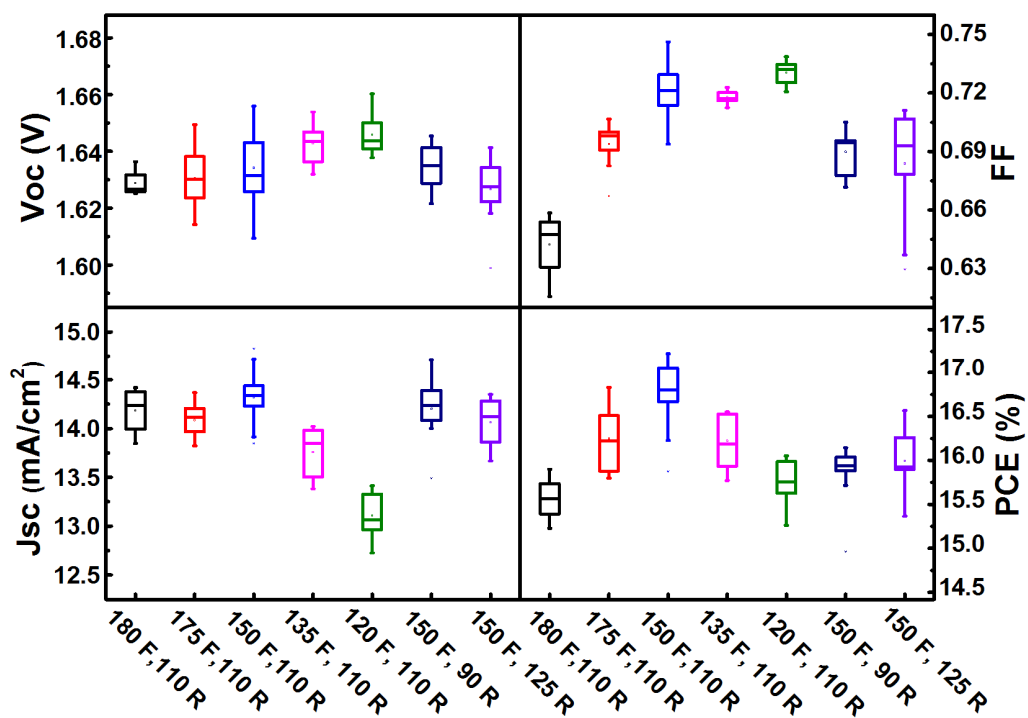


Fig. S8. Photovoltaic parameters (V_{oc} , FF , J_{sc} , PCE) of the tandem devices with different thickness of the subcells (F refers to the front cell, R refers to the rear cell).



TEST REPORT

No. :2017DMCS00062

PRODUCT NAME Tandem OSC C
TYPE/MODEL ---
CUSTOMER Nankai University



National Center of Supervision & Inspection on Solar Photovoltaic Products Quality



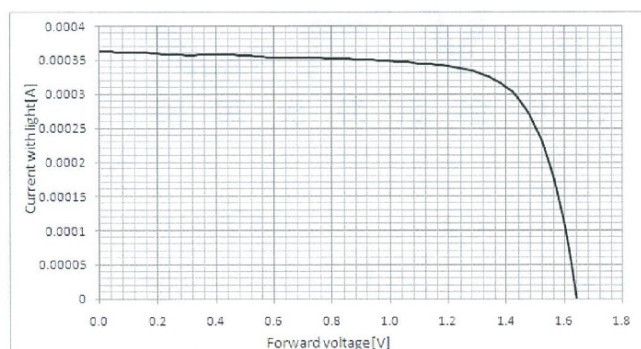
Test Results

No:2017DMCS00062

Page 4 of 4

Clause	Test item(s)	Unit	Technical requirements	Results	Verdict Pass/Fail
1	Current-voltage characteristic measurement (1#)	---	At STC (cell temperature: 25 °C, irradiance: 1000W/m ² , standard solar spectral irradiance distribution corresponds to IEC60904-3), measure the current-voltage characteristics of the cell with the variation of load	-----	---
1.1	Open-circuit voltage, Voc	V	-----	1.640	---
1.2	Short-circuit current, Isc	mA	-----	0.3630	---
1.3	Maximun-power, Pmax	mW	-----	0.4366	---
1.4	Maximun-power voltage, Vmp	V	-----	1.360	---
1.5	Maximun-power current, Imp	mA	-----	0.3210	---
1.6	Fill factor, F.F. (%)	---	-----	73.33	---
1.7	Calculate conversion efficiency	---	-----	---	---
1.7.1	Conversion efficiency, η (%)	---	$\eta = \frac{P_{max}}{1000W/m^2 \times S} \times 100\%$	17.29	---
1.7.2	Area, S	cm ²	S is determined by the aperture size of the mask attached to the front side of the tested cell, the mask is provided by the customer.	0.02525	---

1# - Current-voltage characteristic at STC



Remark: 1. The sample is emerging cell, and there is no general test standard at present. The test method is agreed with the customer after negotiation, which is based on IEC 60904-1:2006 and customer requirements.

2. Customer requirements:

- (1) A crystalline silicon solar cell is used as reference cell for the test.
- (2) Scanning direction: From Isc to Uoc .
- (3) The sample is tested at non electrically stable state.

Fig. S9. Original images of the OSC certificate results by the National Center of Supervision & Inspection on Solar Photovoltaic Products Quality of China (CPVT). The tandem device is measured with a mask of 2.525 mm². The tandem device offers a PCE of 17.29%.

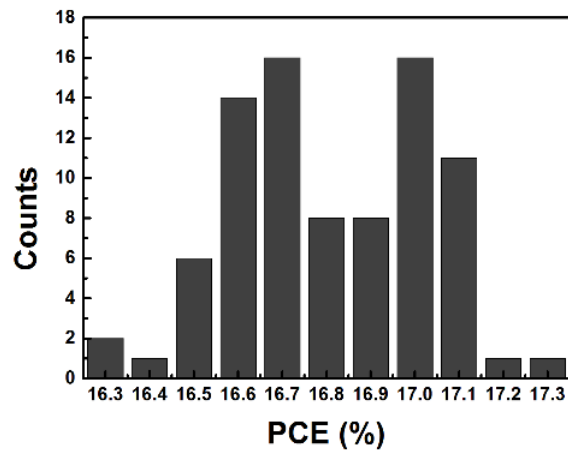


Fig. S10. Histogram of PCE counts for 84 independent cells with a standard deviation of 0.29%.

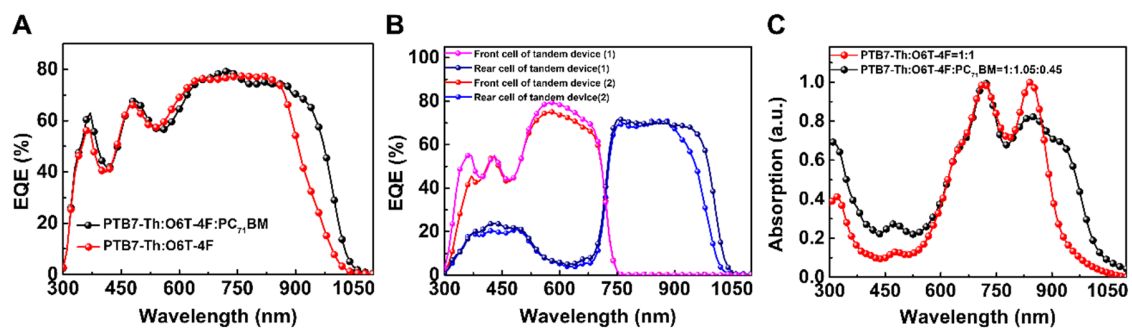


Fig. S11. Photovoltaic performance of the single and tandem devices. (A) EQE curves of the single-junction devices based on PTB7-Th:O6T-4F and PTB7-Th:O6T-4F:PC₇₁BM with an architecture of ITO/ZnO/active layer/MoO₃/Ag. (B) EQE of the optimized tandem devices with PTB7-Th:O6T-4F:PC₇₁BM as rear cell and PTB7-Th:O6T-4F as rear cell. (C) Normalized absorption spectra of PTB7-Th:O6T-4F (1:1) and PTB7-Th:O6T-4F:PC₇₁BM (1:1.05:0.45) films.

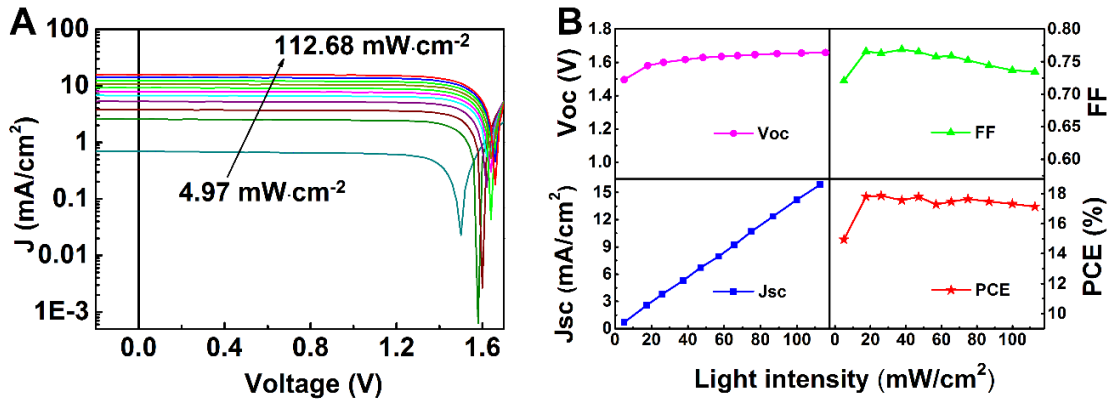


Fig. S12. Tandem device performance parameters under different light intensities. (A) J - V curve of the tandem devices under different light intensity from 4.97 to 112.68 mW/cm². (B) Variation of V_{oc} , FF , J_{sc} and PCE of the tandem device under different light intensities from 4.97 to 112.68 mW/cm².

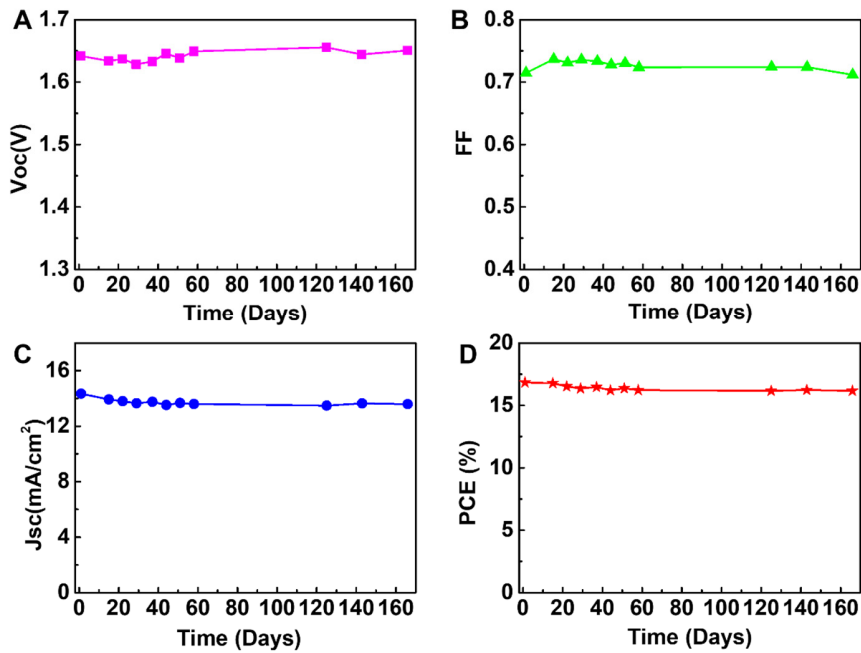


Fig. S13. Stability of the tandem devices. The device performance degraded about 4% after 166 days. Variation of V_{oc} (A), FF (B), J_{sc} (C) and PCE (D) of the tandem device with the time-testing.

Tables

Table S1. The photovoltaic performance of the single-junction devices based on PBDB-T:F-M and PTB7-Th:O6T-4F:PC₇₁BM under illumination of AM 1.5 G, 100 mW/cm².^a

Active layer	V_{oc} (V)	J_{sc} (mA/cm ²)	FF (%)	PCE (%)
PBDB-T:F-M ^b	0.934±0.005 (0.938)	15.86±0.12 (15.96)	69.2±0.5 (69.8)	10.25±0.14 (10.45)
PTB7-Th:O6T-4F ^c	0.703±0.005 (0.705)	25.50±0.38 (25.63)	65.9±0.5 (66.3)	11.59±0.27 (11.93)
PBT7-Th:O6T4F:PC ₇₁ BM ^c	0.689±0.004 (0.691)	27.98±0.35 (27.60)	68.6±0.6 (69.7)	13.22±0.23 (13.29)

^aThe average values are obtained from over 50 devices for each single junction device, and the best PCEs are provided in parentheses. ^bThe device architecture is ITO/ZnO/PFN-Br/active layer/M-PEDOT/Ag. ^cThe device architecture is ITO/ZnO/active layer/MoO₃/Ag.

Table S2. Optimization of D/A ratio for PBDB-T:F-M conventional solar cells under illumination of AM 1.5 G, 100 mW/cm².^a

D/A ratio	V_{oc} (V)	J_{sc} (mA/cm ²)	FF (%)	PCE (%) ^b
1:0.5	0.950	13.56	62.7	8.08
1:0.8	0.964	14.79	63.1	9.00
1:1	0.970	14.85	65.0	9.36
1:1.2	0.981	14.23	64.2	8.96
1:1.5	0.973	14.38	61.6	8.62

^aThe device architecture is ITO/PEDOT:PSS/PBDB-T:F-M/PDINO/Al; D=10 mg/mL in CB with 0.5 vol% DIO; 1500 rpm for 40 s. ^bThe average values are obtained from over 10 devices.

Table S3. Optimization of different additive for PBDB-T:F-M conventional solar cells under illumination of AM 1.5 G, 100 mW/cm².^a

Additives	V_{oc} (V)	J_{sc} (mA/cm ²)	FF (%)	PCE (%) ^b
no	0.990	14.46	67.2	9.62
1-methylnaphthalene	0.975	14.41	54.5	7.66
1,5-Naphthalenedithiol	0.991	14.80	62.8	9.21
Naphthalene	0.988	13.98	66.1	9.13
DIO	0.992	14.94	67.0	9.93

^aThe device architecture is ITO/PEDOT:PSS/PBDB-T:F-M/PDINO/Al; D:A=1:1; D=10 mg/mL in CB with 0.5 vol% additive; 1500 rpm for 40 s. ^bThe average values are obtained from over 10 devices.

Table S4. Optimization of DIO content for PBDB-T:F-M conventional solar cells under illumination of AM 1.5 G, 100 mW/cm².^a

DIO (vol%)	V_{oc} (V)	J_{sc} (mA/cm ²)	FF (%)	PCE (%) ^b
None	0.986	14.33	67.5	9.54
0.1	0.983	15.24	67.2	10.07
0.3	0.986	14.86	70.0	10.26
0.5	0.979	14.36	68.3	9.60
1	0.971	12.94	65.3	8.20

^aThe device architecture is ITO/PEDOT:PSS/PBDB-T:F-M/PDINO/Al; D:A=1:1; D=10 mg/mL in CB with DIO; 1500 rpm for 40 s. ^bThe average values are obtained from over 10 devices.

Table S5. Optimization of different concentration for PBDB-T:F-M conventional solar cells under illumination of AM 1.5 G, 100 mW/cm².^a

Concentration (mg/mL)	V_{oc} (V)	J_{sc} (mA/cm ²)	FF (%)	PCE (%) ^b
20	0.996	14.28	70.7	10.06
22	0.987	14.35	69.9	9.90
24	0.982	14.47	69.4	9.86

^aThe device architecture is ITO/PEDOT:PSS/PBDB-T:F-M/PDINO/Al; D:A=1:1 in CB with 0.2% DIO; 1500 rpm for 40 s. ^bThe average values are obtained from over 10 devices.

Table S6. Optimization of different spin speed for PBDB-T:F-M inverted solar cells under illumination of AM 1.5 G, 100 mW/cm².^a

Spin speed (rpm)	V_{oc} (V)	J_{sc} (mA/cm ²)	FF (%)	PCE (%) ^b
1000	0.938	15.96	69.8	10.45
1200	0.942	15.47	70.2	10.23
1500	0.940	14.91	72.2	10.12
2000	0.938	14.32	73.5	9.87

^aThe device architecture is ITO/ZnO/PFN-Br/PBDB-T:F-M/M-PEDOT/Ag; D:A=1:1, D=10 mg/mL in CB with 0.2% DIO. ^bThe average values are obtained from over 10 devices.

Table S7. Photovoltaic performance of the tandem solar cells with the different concentration of ZnO NPs under illumination of AM 1.5 G, 100 mW/cm².^a

ZnO NPs (mg/mL)	V_{oc} (V)	J_{sc} (mA/cm ²)	FF (%)	PCE (%) ^b
6	1.641	13.97	69.4	15.91
8	1.640	13.99	69.9	16.04
10	1.641	14.11	70.6	16.35
12	1.638	14.15	70.4	16.32
15	1.640	13.78	72.0	16.27
20	1.637	13.64	72.4	16.17

^aThe device architecture is ITO/ZnO/PFN-Br/PBDB-T:F-M/M-PEDOT/ZnO/PTB7-Th:O6T-4F:PC₇₁BM/MoO₃/Ag; ^bfor the PBDB-T:F-M (1:1), PBDB-T=10 mg/mL with 0.2% DIO, 1000 rpm; for the PTB7-Th:O6T-4F:PC₇₁BM (1:1.05:0.45), PTB7-Th=7.2 mg/mL with 1% DIO, 1600 rpm; ZnO Sol-Gel:10 mg/mL with spin speed of 3000 rpm; PFN-Br: 1 mg/mL with 5000 rpm, the spin speed of M-PEDOT and ZnO NPs is 4000 rpm and 3000 rpm; The average values are obtained from over 15 devices.

Table S8. Photovoltaic performance of the tandem solar cells with the different spin speed of ZnO NPs under illumination of AM 1.5 G, 100 mW/cm².^a

Spin speed (rpm)	V_{oc} (V)	J_{sc} (mA/cm ²)	FF (%)	PCE (%) ^b
2000	1.638	14.20	71.3	16.58
3000	1.639	14.01	71.5	16.42
4000	1.641	13.97	71.2	16.32
5000	1.641	13.80	71.1	16.10

^aThe device architecture is ITO/ZnO/PFN-Br/PBDB-T:F-M/M-PEDOT/ZnO/PTB7-Th:O6T-4F:PC₇₁BM/MoO₃/Ag; ^bfor the PBDB-T:F-M (1:1), PBDB-T=10 mg/mL with 0.2% DIO, 1000 rpm; for the PTB7-Th:O6T-4F:PC₇₁BM (1: 1.05:0.45), PTB7-Th =7.2 mg/mL with 1% DIO, 1600 rpm; ZnO Sol-Gel:10 mg/mL with spin speed of 3000 rpm; PFN-Br:1mg/mL with 5000 rpm, the spin speed of M-PEDOT is 4000 rpm and the concentration of ZnO NPs is 12 mg/mL; The average values are obtained from over 15 devices.

Table S9. Photovoltaic performance of the tandem solar cells with the different spin speed of M-PEDOT under illumination of AM 1.5 G, 100 mW/cm².^a

Spin speed (rpm)	V_{oc} (V)	J_{sc} (mA/cm ²)	FF (%)	PCE (%) ^b
3000	1.645	14.18	70.7	16.49
4000	1.641	14.22	71.2	16.61
5000	1.645	14.29	71.4	16.78

^aThe device architecture is ITO/ZnO/PFN-Br/PBDB-T:F-M/M-PEDOT/ZnO/PTB7-Th:O6T-4F:PC₇₁BM/MoO₃/Ag; ^bfor the PBDB-T:F-M (1:1), PBDB-T=10 mg/mL with 0.2% DIO, 1000 rpm; for the PTB7-Th:O6T-4F:PC₇₁BM (1: 1.05:0.45), PTB7-Th =7.2 mg/mL with 1% DIO, 1600 rpm; ZnO Sol-Gel:10 mg/mL with spin speed of 3000 rpm; PFN-Br:1 mg/mL with 5000 rpm, the concentration of ZnO NPs is 12 mg/mL with spin speed of 2000 rpm; The average values are obtained from over 15 devices.

Table S10. Photovoltaic performance of the tandem solar cells with the different concentration of ZnO Sol-Gel under illumination of AM 1.5 G, 100 mW/cm².^a

Concentration (mg/mL)	V_{oc} (V)	J_{sc} (mA/cm ²)	FF (%)	PCE (%) ^b
5	1.642	14.23	68.9	16.10
10	1.644	14.21	71.7	16.75
20	1.638	13.98	72.2	16.53
30	1.640	13.63	71.5	15.98
40	1.640	13.44	71.9	15.85

^aThe device architecture is ITO/ZnO/PFN-Br/PBDB-T:F-M/M-PEDOT/ZnO/PTB7-Th:O6T-4F:PC₇₁BM/MoO₃/Ag; ^bfor the PBDB-T:F-M (1:1), PBDB-T=10 mg/mL with 0.2% DIO, 1000 rpm; for the PTB7-Th:O6T-4F:PC₇₁BM (1: 1.05:0.45), PTB7-Th =7.2 mg/mL with 1% DIO, 1600 rpm; ZnO Sol-Gel with spin speed of 3000 rpm; PFN-Br:1 mg/mL with 5000 rpm; M-PEDOT with a spin speed of 4000 rpm; the concentration of ZnO NPs is 12 mg/mL with spin speed of 2000 rpm; The average values are obtained from over 15 devices.

Table S11. Photovoltaic performance of the tandem solar cells with the different spin speed of ZnO Sol-Gel under illumination of AM 1.5 G, 100 mW/cm².^a

Spin speed (rpm)	V_{oc} (V)	J_{sc} (mA/cm ²)	FF (%)	PCE (%) ^b
2000	1.642	14.12	71.4	16.55
3000	1.641	14.23	71.8	16.77
4000	1.639	14.17	71.2	16.54
5000	1.641	14.02	71.0	16.33

^aThe device architecture is ITO/ZnO/PFN-Br/PBDB-T:F-M/M-PEDOT/ZnO/PTB7-Th:O6T-4F:PC₇₁BM/MoO₃/Ag; ^bfor the PBDB-T:F-M (1:1), PBDB-T=10 mg/mL with 0.2% DIO, 1000 rpm; for the PTB7-Th:O6T-4F:PC₇₁BM (1: 1.05:0.45), PTB7-Th =7.2 mg/mL with 1% DIO, 1600 rpm; ZnO Sol-Gel:10 mg/mL; PFN-Br:1 mg/mL with 5000 rpm; M-PEDOT with a spin speed of 4000 rpm; the concentration of ZnO NPs is 12 mg/mL with spin speed of 2000 rpm; The average values are obtained from over 15 devices.

Table S12. Photovoltaic performance of the tandem solar cells with different spin speed of rear cell under illumination of AM 1.5 G, 100 mW/cm².^a

Spin speed (rpm)	V_{oc} (V)	J_{sc} (mA/cm ²)	FF (%)	PCE(%) ^b
1400	1.635	14.08	69.9	16.09
1600	1.636	14.32	72.1	16.89
2000	1.636	14.03	69.1	15.86

^aThe device architecture is ITO/ZnO/PFN-Br/PBDB-T:F-M/M-PEDOT/ZnO/PTB7-Th:O6T-4F:PC₇₁BM/MoO₃/Ag; ^bfor the PBDB-T:F-M (1:1), PBDB-T=10 mg/mL with 0.2% DIO, 1000 rpm; for the PTB7-Th:O6T-4F:PC₇₁BM (1:1.05:0.45), PTB7-Th =7.2 mg/mL with 1% DIO; ZnO Sol-Gel:10 mg/mL with spin speed of 3000 rpm; PFN-Br:1 mg/mL with 5000 rpm; M-PEDOT with a spin speed of 4000 rpm; the concentration of ZnO NPs is 12 mg/mL with spin speed of 2000 rpm; The average values are obtained from over 15 devices.

Table S13. Photovoltaic performance of the tandem solar cells with different spin speed of front cell under illumination of AM 1.5 G, 100 mW/cm².^a

Spin speed (rpm)	V_{oc} (V)	J_{sc} (mA/cm ²)	FF (%)	PCE (%) ^b
1000	1.636	14.32	72.1	16.89
1200	1.634	13.76	71.2	16.01
1500	1.646	13.11	73.0	15.75

^aThe device architecture is ITO/ZnO/PFN-Br/PBDB-T:F-M/M-PEDOT/ZnO/PTB7-Th:O6T-4F:PC₇₁BM/MoO₃/Ag; ^bfor the PBDB-T:F-M (1:1), PBDB-T=10 mg/mL with 0.2% DIO, 1000 rpm; for the PTB7-Th:O6T-4F:PC₇₁BM (1:1.05:0.45), PTB7-Th =7.2 mg/mL with 1% DIO,1600 rpm; ZnO Sol-Gel:10 mg/mL with spin speed of 3000 rpm; PFN-Br:1 mg/mL with 5000 rpm; M-PEDOT with a spin speed of 4000 rpm; the concentration of ZnO NPs is 12 mg/mL with spin speed of 2000 rpm; The average values are obtained from over 15 devices.

Table S14. Average photovoltaic performance parameters for the optimized tandem devices with different areas under illumination of AM 1.5 G, 100 mW/cm².^a

Area (mm²)	V_{oc} (V)	J_{sc} (mA/cm²)	FF (%)	PCE (%)^b
4	1.636±0.014	14.32±0.18	72.1±1.4	16.89±0.29
	(1.642)	(14.35)	(73.7)	(17.36)
10	1.636±0.016	13.37±0.07	73.2±0.71	16.04±0.24
	(1.639)	(13.48)	(73.6)	(16.26)
106	1.637±0.017	12.96±0.29	65.5±0.66	13.90±0.57
	(1.639)	(13.17)	(66.8)	(14.42)

^aThe device architecture is ITO/ZnO/PFN-Br/PBDB-T:F-M/M-PEDOT/ZnO/PTB7-Th:O6T-4F:PC₇₁BM/MoO₃/Ag; ^bThe best PCEs are provided in parentheses, and the average values are based over 20 devices.

References and Notes

1. M. C. Scharber, N. S. Sariciftci, Efficiency of bulk-heterojunction organic solar cells. *Prog. Polym. Sci.* **38**, 1929–1940 (2013). [doi:10.1016/j.progpolymsci.2013.05.001](https://doi.org/10.1016/j.progpolymsci.2013.05.001) [Medline](#)
2. A. Polman, M. Knight, E. C. Garnett, B. Ehrler, W. C. Sinke, Photovoltaic materials: Present efficiencies and future challenges. *Science* **352**, aad4424 (2016). [doi:10.1126/science.aad4424](https://doi.org/10.1126/science.aad4424) [Medline](#)
3. J. Hou, O. Inganäs, R. H. Friend, F. Gao, Organic solar cells based on non-fullerene acceptors. *Nat. Mater.* **17**, 119–128 (2018). [doi:10.1038/nmat5063](https://doi.org/10.1038/nmat5063) [Medline](#)
4. Z. Xiao, X. Jia, L. Ding, Ternary organic solar cells offer 14% power conversion efficiency. *Sci. Bull.* **62**, 1562–1564 (2017). [doi:10.1016/j.scib.2017.11.003](https://doi.org/10.1016/j.scib.2017.11.003)
5. K. Yoshikawa, H. Kawasaki, W. Yoshida, T. Irie, K. Konishi, K. Nakano, T. Uto, D. Adachi, M. Kanematsu, H. Uzu, K. Yamamoto, Silicon heterojunction solar cell with interdigitated back contacts for a photoconversion efficiency over 26%. *Nat. Energy* **2**, 17032 (2017). [doi:10.1038/nenergy.2017.32](https://doi.org/10.1038/nenergy.2017.32)
6. W. S. Yang, J. H. Noh, N. J. Jeon, Y. C. Kim, S. Ryu, J. Seo, S. I. Seok, SOLAR CELLS. High-performance photovoltaic perovskite layers fabricated through intramolecular exchange. *Science* **348**, 1234–1237 (2015). [doi:10.1126/science.aaa9272](https://doi.org/10.1126/science.aaa9272) [Medline](#)
7. Q. Burlingame, C. Coburn, X. Che, A. Panda, Y. Qu, S. R. Forrest, Centimetre-scale electron diffusion in photoactive organic heterostructures. *Nature* **554**, 77–80 (2018). [doi:10.1038/nature25148](https://doi.org/10.1038/nature25148) [Medline](#)
8. U. Würfel, D. Neher, A. Spies, S. Albrecht, Impact of charge transport on current-voltage characteristics and power-conversion efficiency of organic solar cells. *Nat. Commun.* **6**, 6951 (2015). [doi:10.1038/ncomms7951](https://doi.org/10.1038/ncomms7951) [Medline](#)
9. A. D. Vos, Detailed balance limit of the efficiency of tandem solar cells. *J. Phys. D Appl. Phys.* **13**, 839–846 (1980). [doi:10.1088/0022-3727/13/5/018](https://doi.org/10.1088/0022-3727/13/5/018)
10. G. Li, W.-H. Chang, Y. Yang, Low-bandgap conjugated polymers enabling solution-processable tandem solar cells. *Nat. Rev. Mater.* **2**, 17043 (2017). [doi:10.1038/natrevmats.2017.43](https://doi.org/10.1038/natrevmats.2017.43)
11. Y. Cui, H. Yao, B. Gao, Y. Qin, S. Zhang, B. Yang, C. He, B. Xu, J. Hou, Fine-tuned photoactive and interconnection layers for achieving over 13% efficiency in a fullerene-free tandem organic solar cell. *J. Am. Chem. Soc.* **139**, 7302–7309 (2017). [doi:10.1021/jacs.7b01493](https://doi.org/10.1021/jacs.7b01493) [Medline](#)
12. W. Li, A. Furlan, K. H. Hendriks, M. M. Wienk, R. A. Janssen, Efficient tandem and triple-junction polymer solar cells. *J. Am. Chem. Soc.* **135**, 5529–5532 (2013). [doi:10.1021/ja401434x](https://doi.org/10.1021/ja401434x) [Medline](#)
13. N. Li, C. J. Brabec, Air-processed polymer tandem solar cells with power conversion efficiency exceeding 10%. *Energy Environ. Sci.* **8**, 2902–2909 (2015). [doi:10.1039/C5EE02145F](https://doi.org/10.1039/C5EE02145F)
14. M. Li, K. Gao, X. Wan, Q. Zhang, B. Kan, R. Xia, F. Liu, X. Yang, H. Feng, W. Ni, Y. Wang, J. Peng, H. Zhang, Z. Liang, H.-L. Yip, X. Peng, Y. Cao, Y. Chen, Solution-

- processed organic tandem solar cells with power conversion efficiencies >12%. *Nat. Photonics* **11**, 85–90 (2017). [doi:10.1038/nphoton.2016.240](https://doi.org/10.1038/nphoton.2016.240)
15. J. Y. Kim, K. Lee, N. E. Coates, D. Moses, T. Q. Nguyen, M. Dante, A. J. Heeger, Efficient tandem polymer solar cells fabricated by all-solution processing. *Science* **317**, 222–225 (2007). [doi:10.1126/science.1141711](https://doi.org/10.1126/science.1141711) [Medline](#)
 16. P. Cheng, G. Li, X. Zhan, Y. Yang, Next-generation organic photovoltaics based on non-fullerene acceptors. *Nat. Photonics* **12**, 131–142 (2018). [doi:10.1038/s41566-018-0104-9](https://doi.org/10.1038/s41566-018-0104-9)
 17. Y. J. Cheng, S. H. Yang, C. S. Hsu, Synthesis of conjugated polymers for organic solar cell applications. *Chem. Rev.* **109**, 5868–5923 (2009). [doi:10.1021/cr900182s](https://doi.org/10.1021/cr900182s) [Medline](#)
 18. Z. B. Henson, K. Müllen, G. C. Bazan, Design strategies for organic semiconductors beyond the molecular formula. *Nat. Chem.* **4**, 699–704 (2012). [doi:10.1038/nchem.1422](https://doi.org/10.1038/nchem.1422) [Medline](#)
 19. L. Zuo, X. Shi, S. B. Jo, Y. Liu, F. Lin, A. K. Jen, Tackling energy loss for high-efficiency organic solar cells with integrated multiple strategies. *Adv. Mater.* **30**, e1706816 (2018). [doi:10.1002/adma.201706816](https://doi.org/10.1002/adma.201706816) [Medline](#)
 20. T. Ameri, N. Li, C. J. Brabec, Highly efficient organic tandem solar cells: A follow up review. *Energy Environ. Sci.* **6**, 2390–2413 (2013). [doi:10.1039/c3ee40388b](https://doi.org/10.1039/c3ee40388b)
 21. W. Shockley, H. J. Queisser, Detailed balance limit of efficiency of p-n junction solar cells. *J. Appl. Phys.* **32**, 510–519 (1961). [doi:10.1063/1.1736034](https://doi.org/10.1063/1.1736034)
 22. G. Dennler, M. C. Scharber, T. Ameri, P. Denk, K. Forberich, C. Waldauf, C. J. Brabec, Design rules for donors in bulk-heterojunction tandem solar cells-towards 15% energy-conversion efficiency. *Adv. Mater.* **20**, 579–583 (2008). [doi:10.1002/adma.200702337](https://doi.org/10.1002/adma.200702337)
 23. S. Matthew Menke, A. Niva, Ran, Guillermo C. Bazan, R. H. Friend, Understanding energy loss in organic solar cells: Toward a new efficiency regime. *Joule* **2**, 25–35 (2018). [doi:10.1016/j.joule.2017.09.020](https://doi.org/10.1016/j.joule.2017.09.020)
 24. Z. He, B. Xiao, F. Liu, H. Wu, Y. Yang, S. Xiao, C. Wang, T. P. Russell, Y. Cao, Single-junction polymer solar cells with high efficiency and photovoltage. *Nat. Photonics* **9**, 174–179 (2015). [doi:10.1038/nphoton.2015.6](https://doi.org/10.1038/nphoton.2015.6)
 25. X. Guo, N. Zhou, S. J. Lou, J. Smith, D. B. Tice, J. W. Hennek, R. Ponce Ortiz, J. T. Lopez Navarrete, S. Li, J. Strzalka, L. X. Chen, R. P. H. Chang, A. Facchetti, T. J. Marks, Polymer solar cells with enhanced fill factors. *Nat. Photonics* **7**, 825–833 (2013). [doi:10.1038/nphoton.2013.207](https://doi.org/10.1038/nphoton.2013.207)
 26. Z. Yao, X. Liao, K. Gao, F. Lin, X. Xu, X. Shi, L. Zuo, F. Liu, Y. Chen, A. K. Jen, Dithienopicenocarbazole-based acceptors for efficient organic solar cells with optoelectronic response over 1000 nm and an extremely low energy loss. *J. Am. Chem. Soc.* **140**, 2054–2057 (2018). [doi:10.1021/jacs.7b13239](https://doi.org/10.1021/jacs.7b13239) [Medline](#)
 27. J. Liu, S. Chen, D. Qian, B. Gautam, G. Yang, J. Zhao, J. Bergqvist, F. Zhang, W. Ma, H. Ade, O. Inganäs, K. Gundogdu, F. Gao, H. Yan, Fast charge separation in a non-fullerene organic solar cell with a small driving force. *Nat. Energy* **1**, 16089 (2016). [doi:10.1038/nenergy.2016.89](https://doi.org/10.1038/nenergy.2016.89)

28. Q. Zhang, B. Kan, F. Liu, G. Long, X. Wan, X. Chen, Y. Zuo, W. Ni, H. Zhang, M. Li, Z. Hu, F. Huang, Y. Cao, Z. Liang, M. Zhang, T. P. Russell, Y. Chen, Small-molecule solar cells with efficiency over 9%. *Nat. Photonics* **9**, 35–41 (2015).
[doi:10.1038/nphoton.2014.269](https://doi.org/10.1038/nphoton.2014.269)
29. Y. Chen, X. Wan, G. Long, High performance photovoltaic applications using solution-processed small molecules. *Acc. Chem. Res.* **46**, 2645–2655 (2013).
[doi:10.1021/ar400088c](https://doi.org/10.1021/ar400088c) [Medline](#)
30. J. Benduhn, K. Tvingstedt, F. Piersimoni, S. Ullbrich, Y. Fan, M. Tropiano, K. A. McGarry, O. Zeika, M. K. Riede, C. J. Douglas, S. Barlow, S. R. Marder, D. Neher, D. Spoltore, K. Vandewal, Intrinsic non-radiative voltage losses in fullerene-based organic solar cells. *Nat. Energy* **2**, 17053 (2017). [doi:10.1038/nenergy.2017.53](https://doi.org/10.1038/nenergy.2017.53)
31. Z. Xiao, X. Jia, D. Li, S. Wang, X. Geng, F. Liu, J. Chen, S. Yang, T. P. Russell, L. Ding, 26 mA cm⁻² J_{sc} from organic solar cells with a low-bandgap nonfullerene acceptor. *Sci. Bull.* **62**, 1494–1496 (2017). [doi:10.1016/j.scib.2017.10.017](https://doi.org/10.1016/j.scib.2017.10.017)
32. Y. Zhang, B. Kan, Y. Sun, Y. Wang, R. Xia, X. Ke, Y. Q. Yi, C. Li, H. L. Yip, X. Wan, Y. Cao, Y. Chen, Nonfullerene tandem organic solar cells with high performance of 14.11%. *Adv. Mater.* **30**, e1707508 (2018). [doi:10.1002/adma.201707508](https://doi.org/10.1002/adma.201707508) [Medline](#)
33. G. F. Burkhard, E. T. Hoke, M. D. McGehee, Accounting for interference, scattering, and electrode absorption to make accurate internal quantum efficiency measurements in organic and other thin solar cells. *Adv. Mater.* **22**, 3293–3297 (2010).
[doi:10.1002/adma.201000883](https://doi.org/10.1002/adma.201000883) [Medline](#)
34. R. Timmreck, T. Meyer, J. Gilot, H. Seifert, T. Mueller, A. Furlan, M. M. Wienk, D. Wynands, J. Hohl-Ebinger, W. Warta, R. A. J. Janssen, M. Riede, K. Leo, Characterization of tandem organic solar cells. *Nat. Photonics* **9**, 478–479 (2015).
[doi:10.1038/nphoton.2015.124](https://doi.org/10.1038/nphoton.2015.124)
35. S. Rühle, Tabulated values of the Shockley-Queisser limit for single junction solar cells. *Sol. Energy* **130**, 139–147 (2016). [doi:10.1016/j.solener.2016.02.015](https://doi.org/10.1016/j.solener.2016.02.015)
36. Y. Huang, E. J. Kramer, A. J. Heeger, G. C. Bazan, Bulk heterojunction solar cells: Morphology and performance relationships. *Chem. Rev.* **114**, 7006–7043 (2014).
[doi:10.1021/cr400353v](https://doi.org/10.1021/cr400353v) [Medline](#)
37. Z. A. Page, Y. Liu, V. V. Duzhko, T. P. Russell, T. Emrick, Fulleropyrrolidine interlayers: Tailoring electrodes to raise organic solar cell efficiency. *Science* **346**, 441–444 (2014).
[doi:10.1126/science.1255826](https://doi.org/10.1126/science.1255826) [Medline](#)
38. Z. Wu, C. Sun, S. Dong, X. F. Jiang, S. Wu, H. Wu, H. L. Yip, F. Huang, Y. Cao, n-Type water/alcohol-soluble naphthalene diimide-based conjugated polymers for high-performance polymer solar cells. *J. Am. Chem. Soc.* **138**, 2004–2013 (2016).
[doi:10.1021/jacs.5b12664](https://doi.org/10.1021/jacs.5b12664) [Medline](#)
39. H. Bin, L. Gao, Z. G. Zhang, Y. Yang, Y. Zhang, C. Zhang, S. Chen, L. Xue, C. Yang, M. Xiao, Y. Li, 11.4% Efficiency non-fullerene polymer solar cells with trialkylsilyl substituted 2D-conjugated polymer as donor. *Nat. Commun.* **7**, 13651 (2016).
[doi:10.1038/ncomms13651](https://doi.org/10.1038/ncomms13651) [Medline](#)

40. D. Qian, L. Ye, M. Zhang, Y. Liang, L. Li, Y. Huang, X. Guo, S. Zhang, Z. Tan, J. Hou, Design, application, and morphology study of a new photovoltaic polymer with strong aggregation in solution state. *Macromolecules* **45**, 9611–9617 (2012). [doi:10.1021/ma301900h](https://doi.org/10.1021/ma301900h)
41. W. J. E. Beek, M. M. Wienk, M. Kemerink, X. Yang, R. A. J. Janssen, Hybrid zinc oxide conjugated polymer bulk heterojunction solar cells. *J. Phys. Chem. B* **109**, 9505–9516 (2005). [doi:10.1021/jp050745x](https://doi.org/10.1021/jp050745x) [Medline](#)
42. V. Shrotriya, G. Li, Y. Yao, T. Moriarty, K. Emery, Y. Yang, Accurate measurement and characterization of organic solar cells. *Adv. Funct. Mater.* **16**, 2016–2023 (2006). [doi:10.1002/adfm.200600489](https://doi.org/10.1002/adfm.200600489)
43. N. Qiu, H. Zhang, X. Wan, C. Li, X. Ke, H. Feng, B. Kan, H. Zhang, Q. Zhang, Y. Lu, Y. Chen, A new nonfullerene electron acceptor with a ladder type backbone for high-performance organic solar cells. *Adv. Mater.* **29**, 1604964 (2017). [doi:10.1002/adma.201604964](https://doi.org/10.1002/adma.201604964) [Medline](#)
44. Z. Zhang, B. Qi, Z. Jin, D. Chi, Z. Qi, Y. Li, J. Wang, Perylene Diimides: A thickness-insensitive cathode interlayer for high performance polymer solar cells. *Energy Environ. Sci.* **7**, 1966 (2014). [doi:10.1039/c4ee00022f](https://doi.org/10.1039/c4ee00022f)
45. Z. Zhang, M. Li, Y. Liu, J. Zhang, S. Feng, X. Xu, J. Song, Z. Bo, Simultaneous enhancement of the molecular planarity and the solubility of non-fullerene acceptors: Effect of aliphatic side-chain substitution on the photovoltaic performance. *J. Mater. Chem. A Mater. Energy Sustain.* **5**, 7776–7783 (2017). [doi:10.1039/C7TA02141K](https://doi.org/10.1039/C7TA02141K)
46. J. You, L. Dou, K. Yoshimura, T. Kato, K. Ohya, T. Moriarty, K. Emery, C. C. Chen, J. Gao, G. Li, Y. Yang, A polymer tandem solar cell with 10.6% power conversion efficiency. *Nat. Commun.* **4**, 1446 (2013). [doi:10.1038/ncomms2411](https://doi.org/10.1038/ncomms2411) [Medline](#)
47. S. H. Park, A. Roy, S. Beaupré, S. Cho, N. Coates, J. S. Moon, D. Moses, M. Leclerc, K. Lee, A. J. Heeger, Bulk heterojunction solar cells with internal quantum efficiency approaching 100%. *Nat. Photonics* **3**, 297–302 (2009). [doi:10.1038/nphoton.2009.69](https://doi.org/10.1038/nphoton.2009.69)
48. W. Zhao, S. Li, H. Yao, S. Zhang, Y. Zhang, B. Yang, J. Hou, Molecular optimization enables over 13% efficiency in organic solar cells. *J. Am. Chem. Soc.* **139**, 7148–7151 (2017). [doi:10.1021/jacs.7b02677](https://doi.org/10.1021/jacs.7b02677) [Medline](#)
49. G. Zhang, J. Zhao, P. C. Y. Chow, K. Jiang, J. Zhang, Z. Zhu, J. Zhang, F. Huang, H. Yan, Nonfullerene acceptor molecules for bulk heterojunction organic solar cells. *Chem. Rev.* **118**, 3447–3507 (2018). [doi:10.1021/acs.chemrev.7b00535](https://doi.org/10.1021/acs.chemrev.7b00535) [Medline](#)